Journal of Alloys and Compounds 1038 (2025) 182896

Contents lists available at ScienceDirect

Journal of Alloys and Compounds

journal homepage: www.elsevier.com/locate/jalcom

On the mechanical behavior of additively manufactured AlSi10Mg processed by post heat treatment: The role of hierarchically heterogeneous microstructure

Bo Mao [a,*], Shuangjie Chu [a,b], Sai Chen [a], Xing Zhang [c,*], Yuqian Wang [d], Hui Xing [a], Genqi Tian [a], Jiao Zhang [a,e,f], Baode Sun [a,e,f]

[a] School of Materials Science and Engineering, Shanghai Jiao Tong University, Shanghai 200240, China
[b] Baoshan Iron & Steel Cooperation Limited, Shanghai 201900, China
[c] School of Mechanical and Electric Engineering, Soochow University, Suzhou 215100, China
[d] Department of Mechanical Engineering, University of Nevada-Reno, Reno 89557, USA
[e] State Key Lab of Metal Matrix Composites, Shanghai Jiao Tong University, Shanghai 200240, China
[f] Collaborative Innovation Center for Advanced Ship and Deep-Sea Exploration, Shanghai, Jiao Tong University, Shanghai 200240, China

ARTICLE INFO

Keywords:
Additive manufacturing
AlSi10Mg alloy
Heat treatment
Strain hardening
Heterogeneous microstructure

ABSTRACT

Post heat treatment is an efficient strategy to tailor the mechanical properties of additively manufactured AlSi10Mg alloy. In-depth understanding of microstructure evolution during heat treatment is critical for optimal microstructure design towards desired mechanical properties. In this work, AlSi10Mg alloy was prepared by laser powder bed fusion (LPBF), followed by two heat treatment routines, namely stress relief (SR) and solution treatment (ST). Microstructure characterization revealed the presence of hierarchically heterogeneous microstructure in the as-built (AB) sample, including the heterogeneous grain structure consisted of columnar grain domains and equiaxed grain bands, the non-uniform distribution of geometrically necessary dislocations (GNDs), and the subgrain cellular structure consisted of soft Al cell and hard eutectic phase network. The heterogeneities at both grain- and subgrain-level contributed to a high ultimate tensile strength and an excellent strain-hardening ability, but the presence of hard eutectic phase network resulted in an unsatisfied ductility. With SR heat treatment, the heterogeneities in the grain structure and GND distribution were slightly reduced, whereas the homogenization of subgrain structure partially occurred due to the fragmentation of eutectic phase network, leading to a moderate strain-hardening ability and a high ductility. With ST heat treatment, the heterogeneities in the grain structure and GND distribution were greatly weakened, accompanied by the elimination of cellular structure, resulting in a low strength and relatively weak strain-hardening ability. This work provides valuable insights into tuning the heat treatment routine to obtain optimal hierarchically heterogeneous microstructure and thus enhanced strength-ductility synergy for the additively manufactured AlSi10Mg alloy.

1. Introduction

Metal additive manufacturing (AM) techniques have emerged as transformative tools for the fabrication of complex metal components with tailored properties. Among them, laser powder bed fusion (LPBF) has received considerable attention due to its superior resolution and capability to produce lightweight structures with minimal post-processing [1,2]. These advantages have enabled LPBF to be widely adopted in consumer [3], biomedical [4], automotive [5], construction [6], defense [7], and aerospace [8] applications. Aluminum alloys, particularly AlSi10Mg, are considered ideal candidates for LPBF due to their short solidification range, good weldability, and balanced mechanical properties [9,10]. However, LPBF-fabricated AlSi10Mg parts often suffer from limited ductility compared to conventionally manufactured counterparts due to ultrafine and divorced eutectic cellular structure, which hinder their broader application in load-bearing structures [11].

To address this issue, post-process heat treatments are commonly applied to LPBF-fabricated AlSi10Mg components to modify microstructure and relieve residual stress for enhanced mechanical

* Corresponding authors.
E-mail addresses: bmao@sjtu.edu.cn (B. Mao), xingzhang@suda.edu.cn (X. Zhang).

https://doi.org/10.1016/j.jallcom.2025.182896
Received 29 March 2023; Received in revised form 3 July 2025; Accepted 8 August 2025
Available online 8 August 2025

performance. Numerous studies have examined the influence of conventional treatments (e.g. T6 treatment) on microstructure and tensile properties [12–15]. For example, Aboulkhair et al. [16] reported that T6 treatment reduced the yield and ultimate tensile strength of the LPBF-fabricated AlSi10Mg alloy due to the grain corasening. Li et al. [17] showed that continuous eutectic silicon networks accelerated dislocation exhaustion and reduced ductility, whereas partial cellular or non-cellular networks induced by solution treatment lowered the geometrically necessary dislocation (GND) density and reduced strain-hardening rate. Bagherifard et al. [18] also found that the spheroidizated interdendritic silicon structure induced by T6 treatment significantly improved ductility. However, most existing studies implicitly treat the LPBF-fabricated AlSi10Mg microstructure as structurally uniform, and therefore focus on the isolated effects of grain refining/coarsening, solute diffusion, or precipitate evolution. This oversimplification neglects the intrinsic spatial heterogeneities introduced during rapid solidification, limiting the understanding of how heat treatment governs mechanical behavior.

Recent insights suggest that the mechanical performance of AMed components is not solely governed by grain refining/coarsening or precipitate hardening, but also by multi-level heterogeneities embedded in the solidified microstructure [19,20]. Specifically, at the grain scale, the microstructure could comprise a mixture of columnar grains and equiaxed grains due to variations in thermal gradients and solidification conditions [21]. At a finer structural scale, a cellular network often develops within grains during rapid solidification, comprising soft Al-rich cells surrounded by harder solute-rich walls due to local elemental segregation [22]. These morphological and micro-mechanical contrasts between adjacent regions can lead to local strain incompatibilities, which critically influence both plastic deformation and fracture behavior. Such hierarchically heterogeneous microstructure has been largely overlooked in previous studies. Understanding how this hierarchical architecture evolves under different heat treatment conditions and how it influences the strength-ductility balance is essential for microstructure-guided design of LPBF-fabricated AlSi10Mg alloys.

In this study, we systematically investigate the microstructure evolution and mechanical behavior of LPBF-fabricated AlSi10Mg alloy under two representative post-heat treatment conditions: stress relief (SR) and solution treatment (ST). The evolution of critical microstructure features, including grain structure, subgrain cellular morphology, silicon spheroidization, elemental redistribution, and dislocation density are comprehensively characterized. The mechanical response is evaluated through uniaxial tensile testing, and the relationship between microstructure and fracture behavior is examined. Particular attention is paid to the role of hierarchically heterogeneous microstructure in strain hardening behavior and crack evolution, aiming to provide a deeper mechanistic insight into how heat treatment can be tuned to improve the overall mechanical performance of LPBF-fabricated Al alloys.

2. Experimental procedure

2.1. LPBF process of AlSi10Mg specimen

The AlSi10Mg specimens in this study were fabricated using LPBF, as schematically illustrated in Fig. 1a. The laser power system used in the experiments was a commercial Yttrium fiber laser with a maximum power of 400 W. Plasma-atomized AlSi10Mg powders (Si: 10 %, Mg: 0.3 %, Al: balance, wt%) with an average particle size of around 30 μm were used as the raw materials. During the LPBF experiments, laser beam with a diameter of 200 μm, power of 200 W, and a scanning speed of 300 mm/s were used to remelt the Al alloy powders. The layer thickness and hatch distance were 25 and 200 μm, respectively. A stripe scanning strategy with bidirectional laser scanning was employed during the LPBF process, in which the laser scans back and forth along linear tracks within each layer. To minimize residual stress and microstructural anisotropy, the scanning direction was rotated by 67° between adjacent layers. The scanning direction (SD) and transverse direction (TD) are defined based on the scan path and transverse orientation of the first printed layer, while the building direction (BD) is perpendicular to the deposited layers. Rectangular plates with dimensions of 80 mm (SD) by 80 mm (TD) by 10 mm (BD) were fabricated during the LPBF process.

2.2. Post heat treatment processing

Post heat treatment was carried out in a vacuum furnace filled with argon gas to process the AMed AlSi10Mg plates. In this study, two heat treatments strategies (SR and ST) were utilized. The schematic illustration of the heat treatment routine is shown in Fig. 1b. During the SR process, the samples were heated up to 300℃ with a heating rate of 20℃/min and then held for 2 h followed by air cooling to room temperature. This temperature was selected to relieve residual stress without drastically altering microstructure. During the ST process, the samples were heated up to 500℃ with a heating rate of 20℃/min and then held for 2 h followed by water quenching. This temperature was chosen to promote dissolution of the eutectic network, while minimizing excessive grain growth.

2.3. Mechanical property testing

Dog-bone samples with gauge length of 14 mm, width of 4 mm, and a thickness of 3 mm were cut from the LPBF-fabricated AlSi10Mg plate using a fine milling machine. Subsequently, both surfaces and sides of the dog-bone samples were grinded with sander papers (from grid #300 up to #1200) followed by polishing with 3 μm diamond suspension. The tensile tests were carried out using an Instron universal mechanical testing machine with a strain rate of 0.001/s. The stress and strain curves were measured by a clip-on extensometer and recorded during

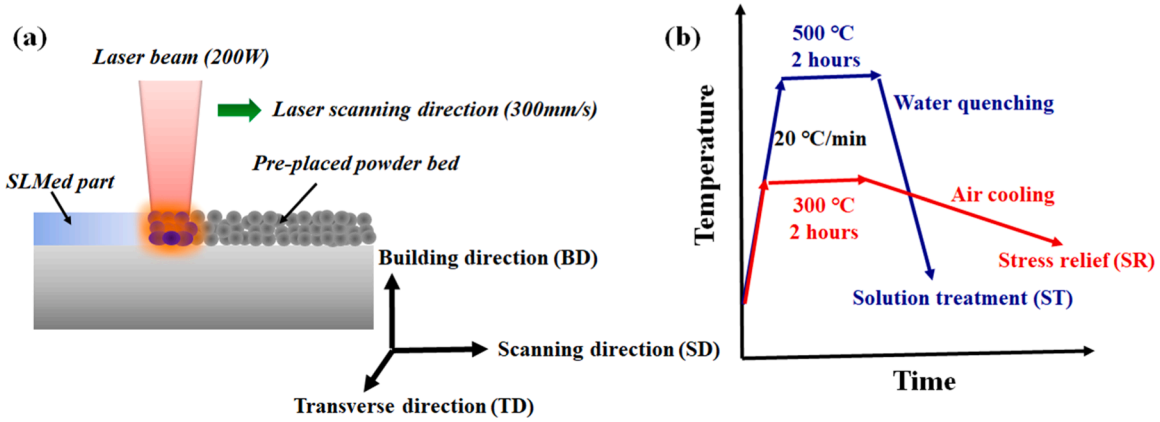

Fig. 1. Schematic illustration of the (a) LPBF process for fabrication of the AlSi10Mg alloy and (b) heat treatment routines for the ST and SR processes.

each tensile test.

2.4. Microstructure characterization

The microstructure of the as-built (AB), SR and ST processed specimens was characterized using optical microscopy (OM), scanning electron microcopy (SEM), and electron backscattered diffraction (EBSD) analysis. To reveal the distribution of the cellular structure, samples were vibrationally polished with 50 nm silica suspension for 8 h, followed by etching with Keller's reagent (2 ml HF, 3 ml HCl, 5 ml HNO_3, and 190 ml H_2O) for 10 s and then subjected to OM and SEM characterization. Energy-dispersive X-ray spectroscopy (EDS) analysis was conducted to characterize the chemical composition of different phases. EBSD analysis was performed at an operating voltage of 20 kV, a working distance of 25 mm, and a sample tilt angle of 70°, for samples before and after tensile testing.

3. Results and discussion

3.1. Mechanical properties of LPBF-fabricated AlSi10Mg via post heat treatment processing

Fig. 2a presents the engineering stress-strain curves of heat-treated (SR, ST) samples along with the non-heat-treated AB sample, and the inset figure displays the fracture samples after tensile failure. The results show that the AB sample exhibits a higher ultimate tensile strength (UTS, 432 MPa) but a lower total elongation (EL, 7.1 %) as compared to the heat-treated samples, which describes the typical strength-ductility trade-off [23]. Comparing between different heat-treated samples, the SR sample has a higher strength (UTS = 252 MPa) but less ductility (EL = 14.2 %) than the ST sample (UTS = 206 MPa, EL = 17.8 %). Moreover, the strain-hardening behavior varies for different samples. It can be found that the AB sample presents an excellent strain-hardening ability, whereas the SR and ST samples show a moderate and low strain-hardening ability, respectively. Fig. 2b depicts the strain-hardening rate after yielding as a function of true strain. For the AB sample, the strain-hardening rate decreases rapidly at the beginning of deformation, then gradually decreases with the increase in strain. Similar trend can be observed for the heat-treated samples, but with a strain-hardening rate at given strains. Additionally, strain hardening lasts until the strain reaches ~5 % for the SR sample, after which strain softening (strain-hardening rate < 0) or necking occurs, whereas necking is absent during straining for the AB and ST samples.

To analyze the tensile failure mode, fracture morphologies of the tensile-tested samples are characterized, as shown in Fig. 3. Fig. 3a-c present the fracture surfaces of AB, SR and ST samples, respectively. The enlarged image in Fig. 3d shows the fracture area of AB sample is dominated by numerous cleavage surfaces, indicating a typical brittle fracture. In contrast, as shown in Figs. 3e and 3f, dimple structures associated with a ductile fracture can be observed in both heat-treated samples. Note that the SR sample exhibits a more ductile failure than the ST sample due to the presence of finer dimples. These results are consistent with the change in the ductility of the AB, SR and ST samples according to the stress-strain behavior in Fig. 2a.

3.2. Microstructure evolution of LBPF-fabricated AlSi10Mg processed by post heat treatment processing

To understand the effect of post heat treatment on the mechanical properties of LBPF-fabricated AlSi10Mg, the macro- and microstructure of all samples are analyzed in the following subsections. Fig. 4 presents the typical macrostructure of AB, SR and ST samples in 3D view, constructed from the surfaces perpendicular to BD, SD and TD directions using OM images. For the AB sample (Fig. 4a), the side-views reveal that the macrostructure exhibit the 'fish-scale' morphology consisting of melt pools with a half-cylindrical shape. The melt pool dimensions are measured to be ~160 μm in width and ~50 μm in height. The top-view reveals laser track segments showing the rotation of laser beam between adjacent layers during the AM process. Such macrostructure becomes less visible after SR at 300 °C, as shown in Fig. 4b. Upon ST at 500 °C (Fig. 4c), the 'fish-scale' morphology and track segments are almost eliminated, showing a relatively homogeneous macrostructure.

Fig. 5 presents the SEM images of the AB sample exhibiting a heterogeneous cellular structure, which is a representative microstructure formed in additively manufactured Al alloys [24]. The microstructure along the BD-SD surface (Fig. 5a) displays the 'fish-scale' patterns, where melt pool (MP) boundaries can be clearly identified (Fig. 5b) due to the microstructural transition across the MP (Fig. 5c). Accordingly, the region near the MP boundary can be divided into two different zones including the coarse grain zone (MP coarse), fine grain zone (MP fine) and transition zone (MP transition). The MP coarse shown in Fig. 5d is composed of rod-like α-Al cells surrounded by a Si-rich eutectic phase network. The average cell size is measured to be ~0.9 μm. The MP fine shown in Fig. 5e occupies most area within the MP and exhibits a microstructure similar to the MP coarse but with a smaller cell size (~0.7 μm). The formation of a thin-layer coarser microstructure could be ascribed to the smaller cooling rate near the MP boundary than in other regions. Similar experimental observations have been reported in other literature [25]. The MP transition shown in Fig. 5f exhibits a cellular structure almost the same as that in the MP fine, except that Si

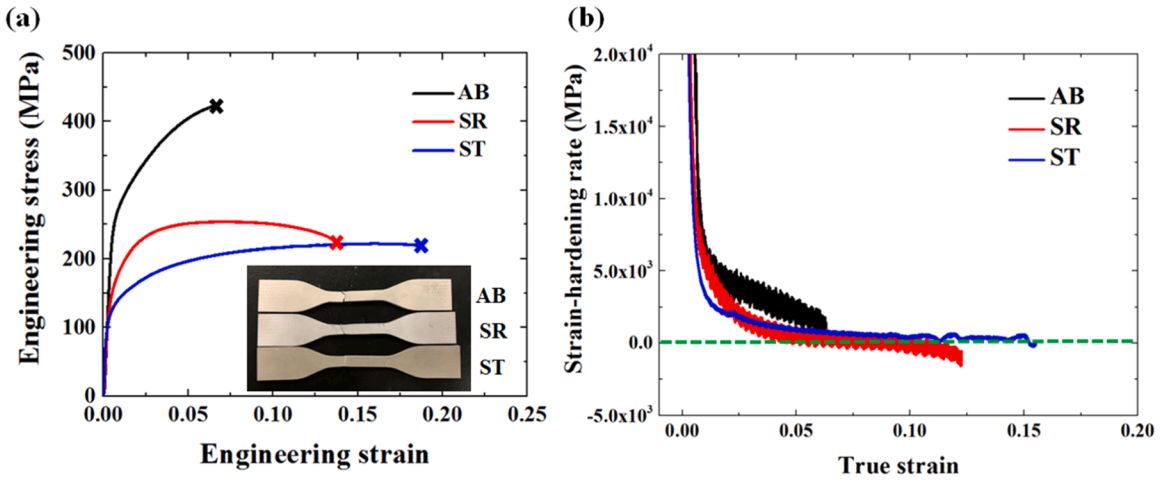

Fig. 2. (a) Engineering stress-strain curves of the AB, SR, and ST samples. The inserted figure shows the lengths of the three specimens after tensile tests. (b) Strain-hardening rates of the AB, SR, and ST processed AlSi10Mg samples during tensile tests.

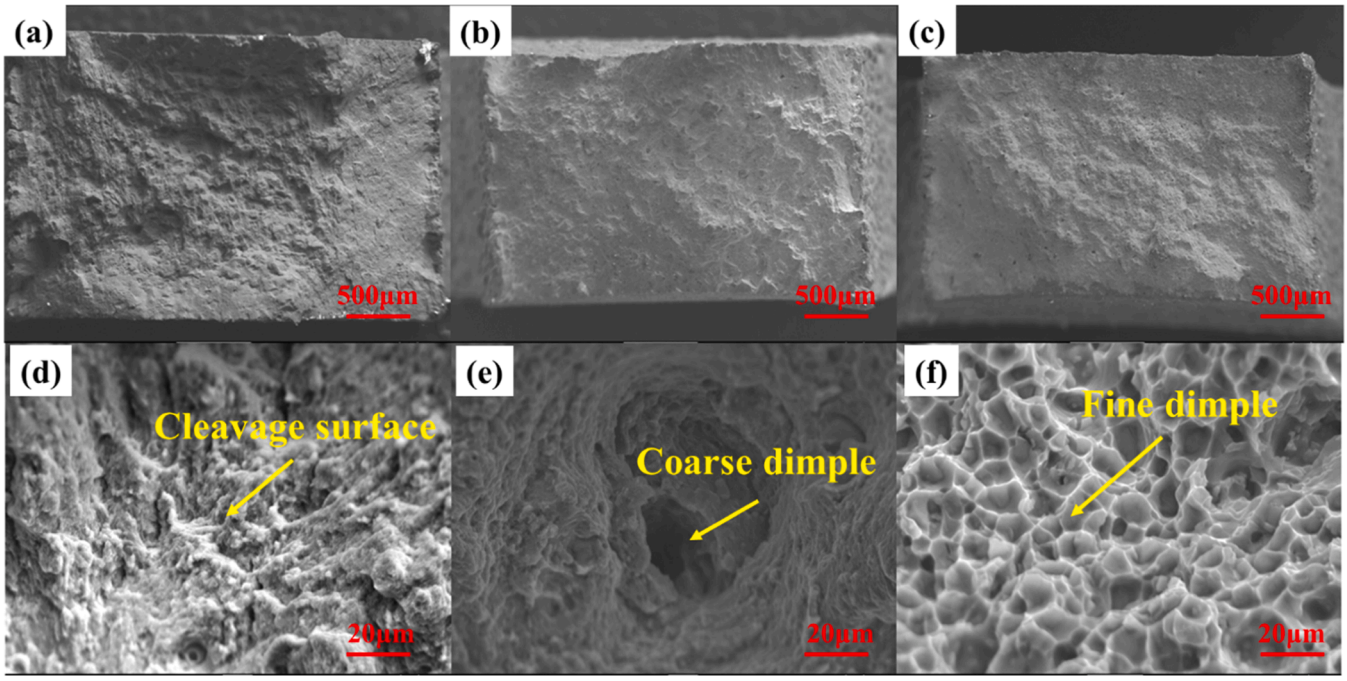

Fig. 3. SEM images of the fracture morphologies after tensile tests: (a) and (d) correspond to the AB samples; (b) and (e) correspond to the SR processed samples; (c) and (f) correspond to the ST processed samples. (a-c) are the SEM images of the fracture surfaces with a low magnification; (d-f) are the magnified fracture surfaces showing different fracture mechanisms.

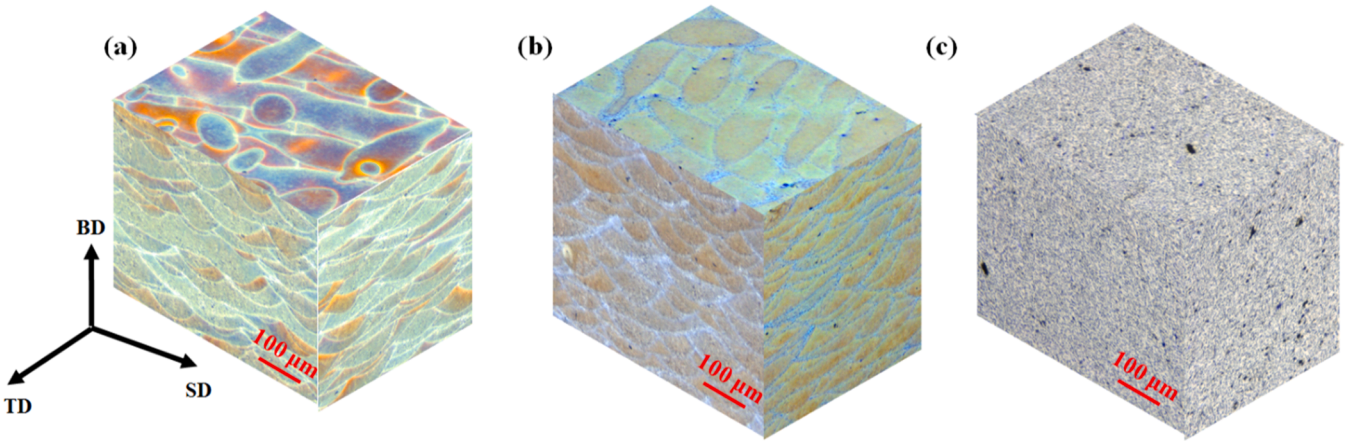

Fig. 4. 3D OM microscopy of the LPBF-fabricated AlSi10Mg specimen: (a) AB, (b) SR and (c) ST processed samples.

precipitates can be observed in the primary α-Al cells. The similar cell size indicates that the MP transition is evolved from the MP fine, which could be explained by the reheating effect in the previously solidified layer during subsequent layer buildup.

Fig. 5g-j displays the cellular structure along the TD-SD surface, exhibiting a honeycomb morphology from the top-view rather than elongated cells from the side-view in Fig. 5d-f. The obvious color contrast within the cellular structure indicates significantly non-uniform elemental distribution in the AB sample. To investigate that, EDS analysis was carried out in the MP coarse, as shown in Fig. 5k-m. The results of EDS mapping reveal that the cell is enriched with Al and the cell boundary is solute (Si) enriched. Such concentration variation between the cell and the cell boundary, also known as microsegregation, is caused by the solute rejection from the solidified cell into the liquid cell boundary during solidification [26]. Further results of point scanning quantitatively reveal the microsegregation behavior, showing that the amount of Si reaches 9.6 wt% inside the α-Al cell and 17.8 wt% within the cell boundary (the eutectic phase network). It is evident that the α-Al cell is supersaturated since the Si concentration greatly exceeds its maximum solubility (1.6 wt%) in the Al matrix [27]. Such non-equilibrium microsegregation is induced by the ultrahigh cooling rate (10^4 - 10^6 K/s [28,29]) during AM that limits the diffusion of solute atoms.

Fig. 6a-d presents the microstructure of the SR sample along the BD-SD surface at different magnifications. In comparison to the AB sample, two zones (MP coarse and MP fine) can be identified near the MP boundary, whereas the MP transition is eliminated during the heat treatment. The enlarged SEM images show that the eutectic network at the cell boundary become fragmented. Meanwhile, numerous nanoscale Si precipitates can be observed along the α-Al cell boundary. Same microstructural change can be found along the TD-SD surface, as shown in Fig. 6e-h, from which the trace of honeycomb morphology is weakly observed. These spheroidizated precipitates are generated through two stages: i) the formation of fine eutectic Si particles in the Si-enriched cell

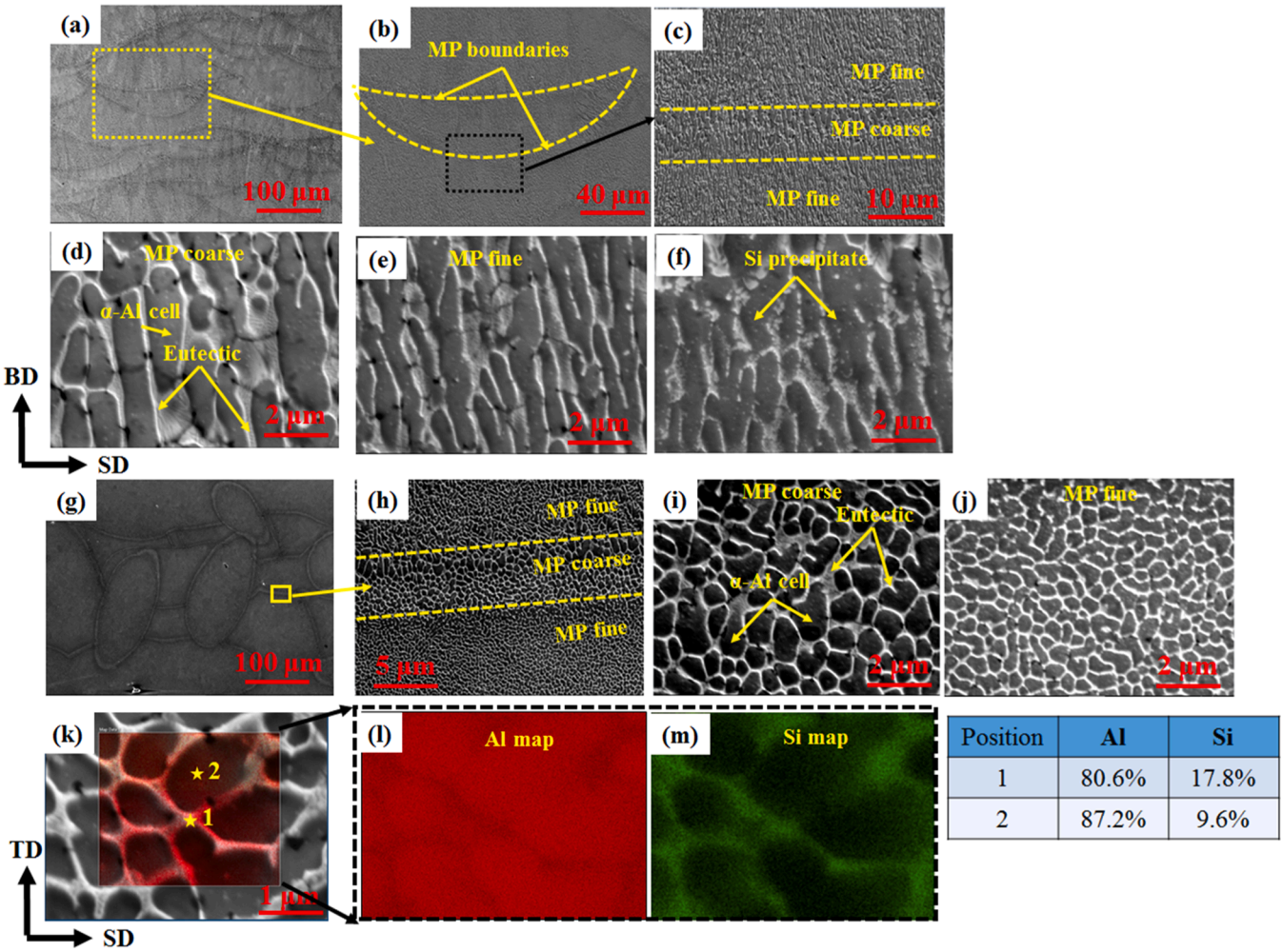

Position	Al	Si
1	80.6%	17.8%
2	87.2%	9.6%

Fig. 5. SEM images of the AB specimen after chemical etching. (a-c): SEM images with a low, medium, and high magnification showing the typical fish-scale patterns, melting pool (MP) boundaries, and subgrain cellular structure; (d-e): microstructure of the coarse grain zone (MP coarse), fine grain zone (MP fine), and transition zone in the BD-SD surface. (g-h): SEM images of the microstructure in the TD-SD surface with different magnifications. (k-m): EDS element maps of the Al (red) and Si (green) for an area in (i).

boundary caused by the activated diffusion of Si at the elevated temperature; ii) the combination of Ostwald ripening and coalescence of fine eutectic Si particles [30]. Thus, the heat treatment is expected to affect the elemental distribution within the cellular structure. EDS analysis results (Fig. 6i-k) indicate that the Si concentration in the supersaturated α-Al cell is decreased from 9.6 wt% to 5.1 wt% after SR at 300 °C, proving that the Si atoms diffuse from the cell into the cell boundary.

Upon ST heat treatment, a completely different microstructure can be obtained, as shown in Fig. 7. SEM observations (Fig. 7a and b) reveal a relatively homogeneous microstructure without the trace of α-Al cells, and the formation of significantly coarsened (microscale) Si precipitates. The EDS analysis results (Fig. 7c) demonstrate that the precipitates contain 93.4 wt% Si and only 6.6 wt% Al, indicating a pronounced long-range diffusion and local accumulation of Si atoms. Moreover, compare to the AB and SR samples, the ST sample exhibits a lower concentration of Si (2.8 wt%) in the Al matrix. This value is close to the equilibrium concentration of Si solute in Al alloys, which means the amount of Si precipitates may remain constant with further heat treatment. The formation of such homogeneous microstructure could be attributed to the following reasons. Upon solution heat treatment, the eutectic phase network and Si precipitates are dissolved, releasing Si atoms into the Al matrix due to the enhanced Si solubility at elevated temperature. Then, during the cooling stage, the decrease of Si solubility in Al induces the precipitation process, leading to the formation of uniformly distributed Si particles.

Next, the microstructural changes as affected by post heat treatment are further investigated by the EBSD analysis, with a focus on the evolution of grain structure. Fig. 8a-c displays the inverse pole figure (IPF) map of the AB, SR and ST samples, respectively, showing grain morphology, size and orientation. It is found that coarse columnar Al grains growing epitaxially towards the MP center are the dominated grain structure within the MP. This is because the grains that have $< 100 >$ crystalline orientations (the preferential solidification directions for α-Al) aligned with the temperature gradient grow much faster than other grains [31]. Beside the columnar grains, a number of fine equiaxed grains could be found near the MP boundary as a result of heterogeneous nucleation at the beginning of rapid solidification. This phenomenon is commonly observed at the mould wall in conventional casting or at the fusion line in welding [32], since the temperature gradient to growth rate ratio is relatively low in these chill zones (large temperature gradient), promoting the formation of equiaxed grain structure. Consequently, a heterogeneous grain structure consisted of columnar grain domains and equiaxed grain bands is observed. The comparison results among all samples show that the characteristics of grain structure remain almost the same after SR heat treatment. Upon ST at 500 °C, the columnar grains still dominate the microstructure, whereas the number of equiaxed grain is significantly reduced,

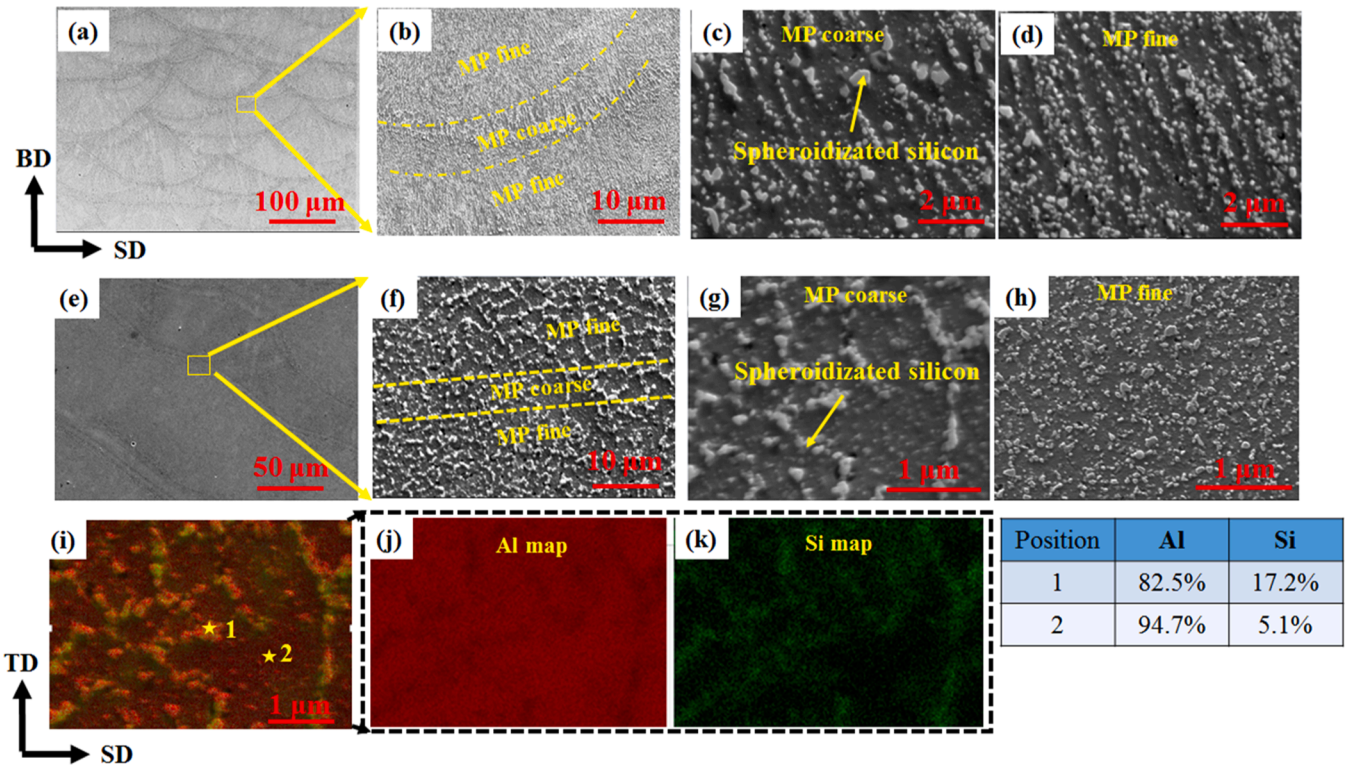

Position	Al	Si
1	82.5%	17.2%
2	94.7%	5.1%

Fig. 6. SEM images of the SR specimen after chemical etching. (a-d): SEM images with a low, medium, and high magnification showing the typical fish-scale patterns, melting pool (MP) boundaries, and hierarchical structure in the BD-SD surface. (e-h): SEM images of the microstructure in the TD-SD surface with different magnifications. (i-k): EDS element maps of the Al (red) and Si (green) for (g).

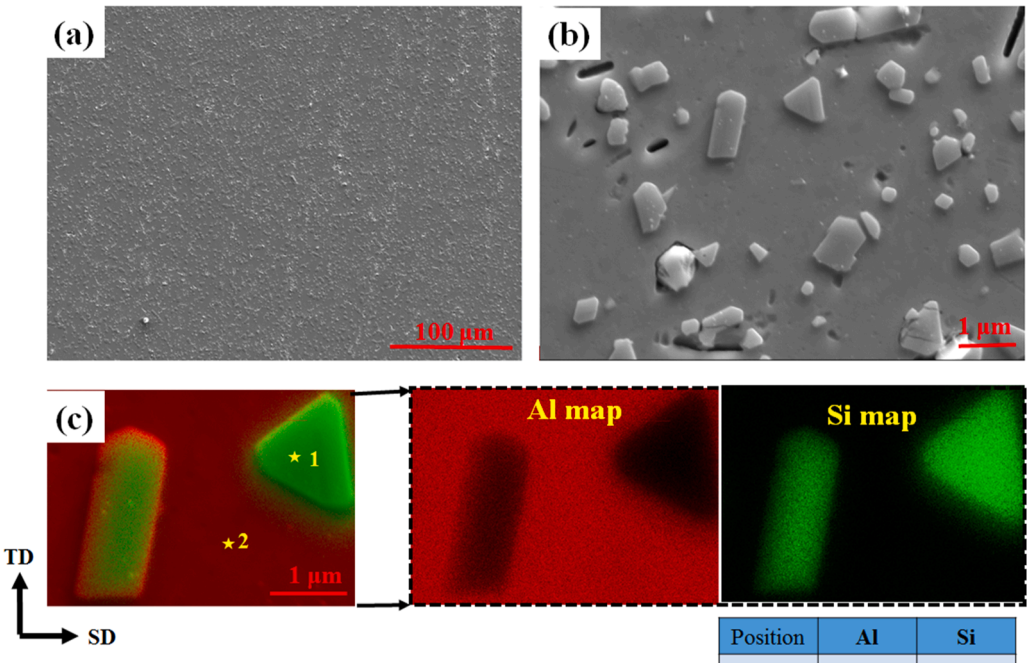

Position	Al	Si
1	6.6%	93.4%
2	94.3%	2.8%

Fig. 7. SEM images of the ST specimen after chemical etching. (a, b): SEM images with a low and high magnification showing the distribution of silicon. (c) EDS element maps of the Al (red) and Si (green) for an area in (b).

demonstrating the coalescence of small grains at elevated temperature.

Fig. 8d-f presents kernel average misorientation (KAM) maps of the AB, SR and ST samples, respectively, with local misorientation angles ranging from 0°to 5°. KAM is often used to assess the distributions of local strain and geometrically necessary dislocations (GNDs). Based on the KAM maps, heterogeneous distribution of local misorientation can

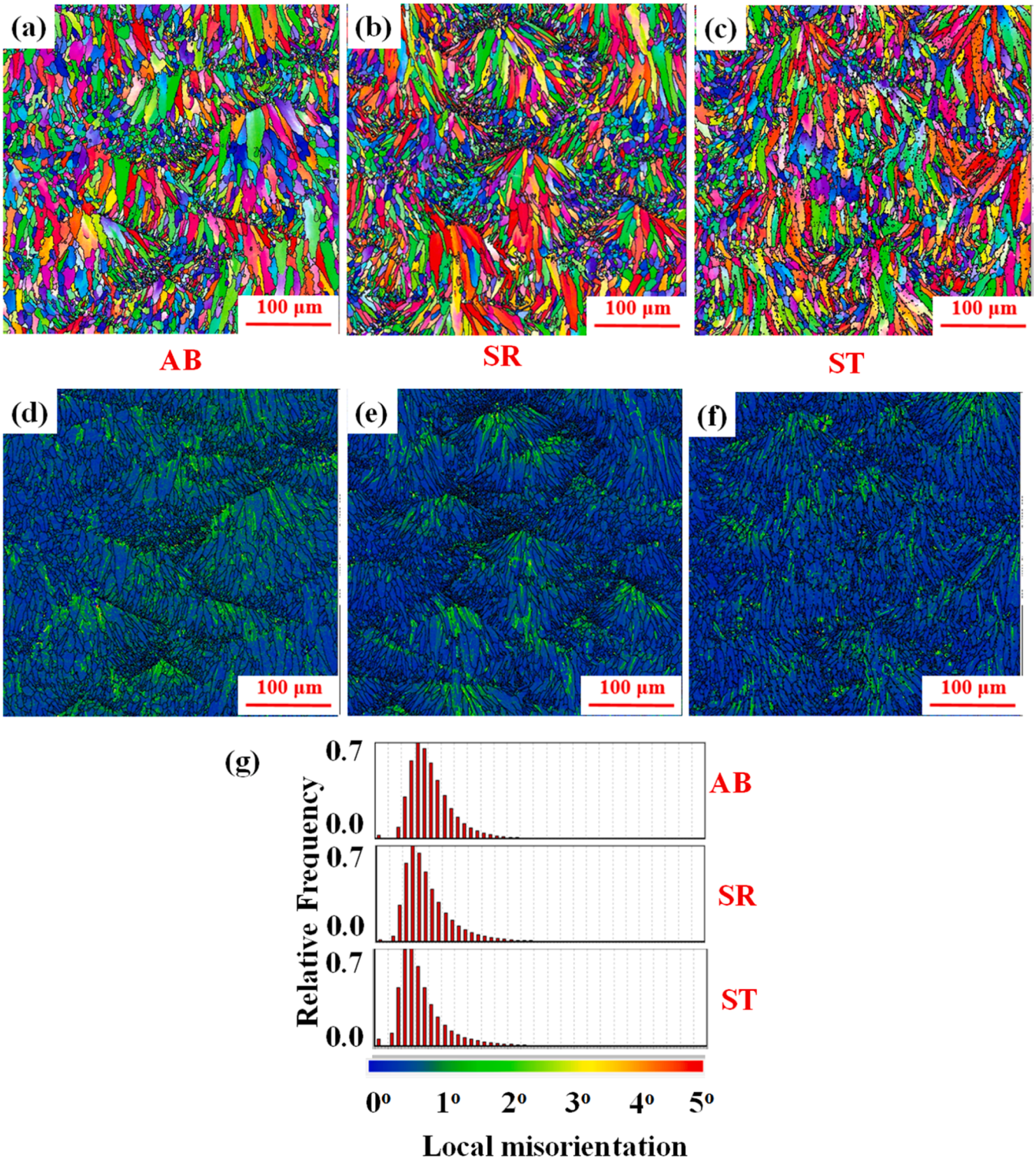

Fig. 8. IPF maps of the (a) AB, (b) SR, and (c) ST samples. Local misorientation map of the (d) AB, (e) SR, and (f) ST samples. (g) A comparison of the local misorientation histogram for the three samples.

be observed in all three samples, with the yellow and green colored areas representing accumulated strain or GNDs. In the AB sample (Fig. 8d), local misorientations are presented in most areas, indicating a high density of GNDs stored across the material, especially at the grain interiors. This can be explained by the formation of cellular structure during rapid solidification. Upon fast cooling, the large residual stress in the solidified material induces local plastic strain, which is accommodated by GNDs resulting from the different plastic deformation behaviors between the cell (soft phase) and the cell boundary (hard phase with eutectic structure). As a result, the generated GNDs are piled up and retained at the cell boundary, which has been confirmed in other literature [33]. Additionally, the high-strain areas are majorly located near the MP center rather than the boundary due to more dislocation accumulation resulting from the higher cooling rate, which also contributes to the heterogeneity in the microstructure. Upon the SR heat treatment (Fig. 8e), the residual stress is partially relieved, accompanied

by the dislocation annihilation. Consequently, the fraction of high-strain areas is decreased, particularly near the MP boundary where the GND density is relatively low. By contrast, a significantly decreased fraction of high-strain areas (or considerable reduction in GND density) can be found after ST heat treatment (Fig. 8f) due to the elimination of cellular structure and microstructure homogenization demonstrated in Fig. 7. By comparing the quantified misorientation angle distribution as shown in Fig. 8g, it is evident that the local misorientation decreases with increasing the temperature of heat treatment, which also indicates the effectiveness of SR and ST treatments on diminishing local strain or dislocation density in the LPBF-fabricated AlSi10Mg.

3.3. Deformation microstructure of LPBF-fabricated AlSi10Mg processed by post heat treatment processing

The varying microstructural features in the AB, SR and ST samples could response differently under plastic deformation, leading to dissimilar mechanical behaviors in Fig. 2. To investigate that, the grain structures before and after tensile deformation were characterized by EBSD at a low magnification, as shown in Fig. 9. The IPF maps

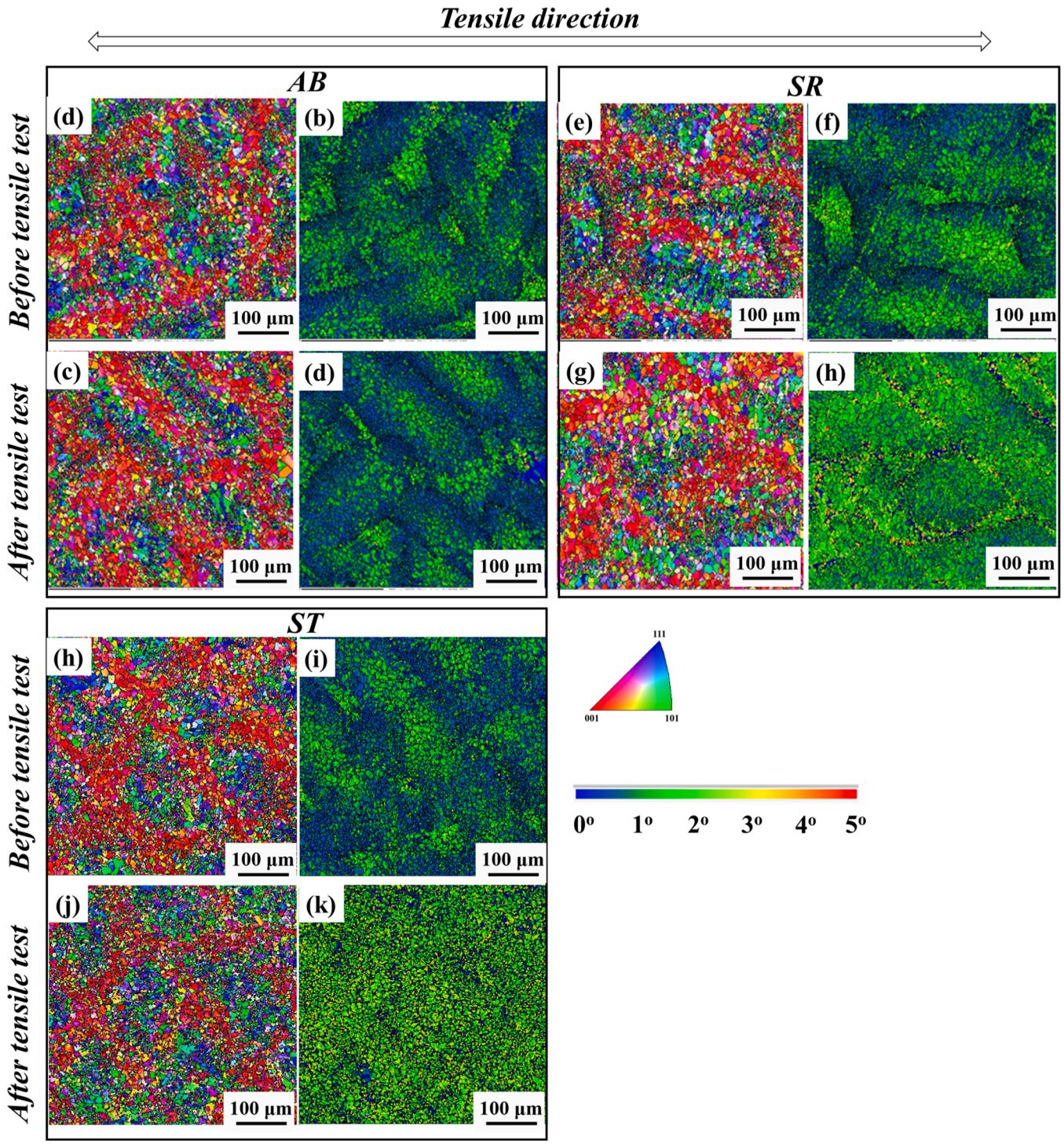

Fig. 9. Comparison of the microstructure and local misorientation distribution for the AB, SR, and ST processed AMed AlSi10Mg specimen before and after tensile tests.

demonstrate no significant change during straining for all samples, proving that grain features including morphology and size do not contribute to the different mechanical responses in this case. Therefore, we further analyzed the KAM maps, which provide insight into local plastic strain and dislocation activity. In the AB sample, high-strain regions with elevated KAM values are already present before loading and show only minor changes after deformation. This indicates a significant degree of pre-existing local strain and deformation inhomogeneity, likely due to the hierarchical microstructure and residual stress introduced during LPBF. In contrast, both SR and ST samples exhibit a marked increase in high-KAM regions after tensile testing. For the SR sample, the high-strain regions expand substantially after loading, indicating post-deformation dislocation accumulation over a wider area. This suggests that the heat treatment partially homogenized the material, allowing for a more distributed but still somewhat localized plastic response. For the ST sample, the high-strain regions become even more uniformly distributed across the scanned area. This reflects a transition toward more homogeneous plastic deformation, which correlates well with the lower strain-hardening rate but improved ductility shown in Fig. 2a. These results support the interpretation that heat treatment progressively reduces deformation heterogeneity, shifting the plastic behavior from localized (AB) to moderately distributed (SR) and ultimately to uniform deformation (ST). This progression is closely linked to the evolution of the hierarchically heterogeneous microstructure and its influence on dislocation storage and propagation mechanisms.

To further reveal the deformation microstructure, a high-magnification EBSD analysis was carried out near the local micro-crack propagation path, as shown in Fig. 10. Figs. 10a and 10b presents a micro-crack with a short length of ~20 μm propagating along the grain boundaries in the AB sample. The corresponding KAM map in Fig. 10c depicts the accumulation and pile-up of high-density GNDs only near the crack region, indicating difficult slip transfer. This could lead to the localized stress concentration at grain boundaries and thus the tendency for intergranular crack propagation. In contrast, for both heat-treated samples (Fig. 10d-i), longer transgranular micro-cracks (length of ~50 and ~100 μm in SR and ST samples, respectively) can be found, indicating higher fracture toughness. Moreover, the accumulation of GNDs across the material proves a more uniform stress distribution under tensile loads, which is consistent with the low-magnification analysis in Fig. 9. Consequently, more regions could withstand the external stress with smaller deformation, leading to the enhanced ductility. This shift from intergranular to transgranular cracking behavior reflects a transition in failure mechanism, from early brittle-like fracture in the AB sample to more ductile, distributed failure in the heat-treated ones. Specifically, intergranular cracks in the AB sample facilitate premature failure by propagating along microstructurally weak paths, thereby limiting post-necking elongation. In contrast, transgranular cracks in the SR and ST samples require higher energy to propagate across grains, which delays fracture and improves ductility. Accordingly, it is reckoned that the different stress/strain or GND distribution is related to the evolution of cellular structure and formation of Si precipitates after post heat treatment, which highly affects the trap and retention of GNDs upon deformation. This will be further discussed in the next subsection.

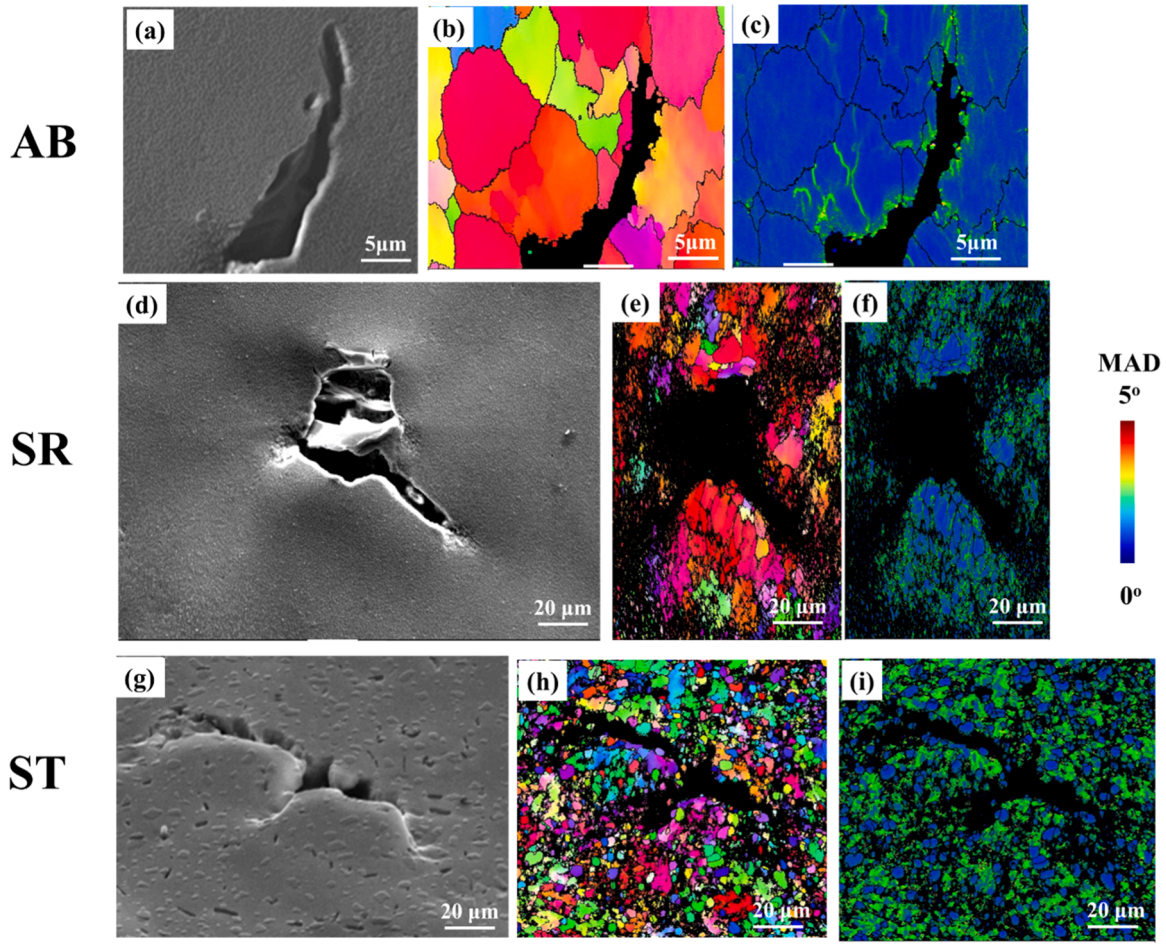

Fig. 10. SEM and EBSD analysis of the surface regime containing micro-cracks in tensile fractured samples: (a-c) analysis for AB sample, (d-f) analysis for SR sample, and (g-i) analysis for ST sample.

3.4. The role of hierarchically heterogeneous microstructure on the mechanical behavior of LPBF-fabricated AlSi10Mg processed by post heat treatment

According to the above experimental results, the effects of heat treatment on the hierarchically heterogeneous microstructure (Fig. 11a) and the resultant mechanical behavior are discussed below. Upon the rapid solidification during the LPBF process, the heterogeneous grain structure consisted of columnar grain domains and equiaxed grain bands are formed due to the larger temperature gradient near the MP boundary, and the non-uniform distribution of initial GNDs are formed due to the higher cooling rate at the MP center. Meanwhile, the subgrain cellular structure consisted of Al cell and Si-enriched eutectic phase network at the cell boundary is also formed as a result of micro-segregation phenomenon. These grain-level and sub-grain-level heterogeneities (Figs. 5 and 8) could introduce variations in local micromechanical response, leading to strain gradient at the hetero-interface upon deformation. Consequently, the generation and accumulation of GNDs occur at the interface (Fig. 11b) to accommodate the strain incompatibility between the soft and hard regions, resulting in the formation of hetero-deformation-induced (HDI) stress. It has been reported [34] that such HDI stress could simultaneously enhance the global material strength via strengthening soft regions and retain the ductility by enhanced strain hardening, which could explain the tensile behavior of AB sample shown in Fig. 2. Moreover, compare to the heterogenous grain structure and dislocation distribution, the subgrain cellular structure presents a higher heterogeneity in the local plasticity due to the large difference in strength between soft Al and hard eutectic phase network. Therefore, it is expected that the cellular structure is a major contributor to the excellent strain-hardening behavior. It is also worth mentioning that the ductility of the AB sample is relatively low as a result of sudden failure without post-necking elongation, which may derive from the hard eutectic phase network functioning as a highway for intergranular crack propagation.

On comparison, after SR heat treatment, the heterogenous grain structure and dislocation distribution are slightly changed, whereas the eutectic phase network of cellular structure become fragmented, which allows the dislocations to penetrate through the interconnected Al regions. This promotes less accumulation of GNDs at the hetero-interfaces (especially at the interface between Al and Si phases, as shown in Fig. 11c) upon deformation, and thus a significant reduction in strength and strain-hardening ability. Note that the precipitating of Si generally leads to a strengthening effect in the as-cast AlSi10Mg alloy, which is contradictory to the reduced strength after SR heat treatment in this study. This further confirms that the high strength and excellent strain-hardening behavior of the AB sample originate from the accumulation of GNDs at hetero-interface. With ST heat treatment, the heterogeneities in the grain structure and dislocation distribution are greatly weakened, and the cellular structure is completely diminished. Consequently, upon deformation, GNDs could only form sparsely near the coarsened Si particles across the material (Fig. 11d), leading to further reduction in strength and strain-hardening ability. Meanwhile, the decreased number of Si particles due to coarsening contributes to more free paths for dislocation movement, resulting in the increased ductility. Note that statistically stored dislocations (SSDs) may also contribute to strain-hardening behavior due to the existence of short-range stress required for dislocation movement [35]. However, the considerable loss of strain-hardening ability after heat treatment confirms that the accumulation of GNDs is the main reason for the excellent strain-hardening behavior in the AB sample. In addition, it is suspected that the strain-hardening behavior in the ST sample is mainly attributed to SSDs since GND density is greatly reduced in the ST sample, and by contrast, the moderate strain-hardening ability in the SR sample could be caused by both GNDs and SSDs.

4. Conclusions

In the current study, the complicated microstructural features of LPBF-fabricated AlSi10Mg alloy and the associated mechanical properties as affected by heat treatment conditions were systematically investigated. The microstructure characterization results indicated considerable hierarchically heterogeneities in the as-built AlSi10Mg alloy, including the heterogeneous grain structure consisted of columnar grain domains and equiaxed grain bands, the non-uniform distribution of initial GNDs, and the subgrain cellular structure consisted of soft Al cell and hard eutectic phase network. Such hierarchically heterogeneous

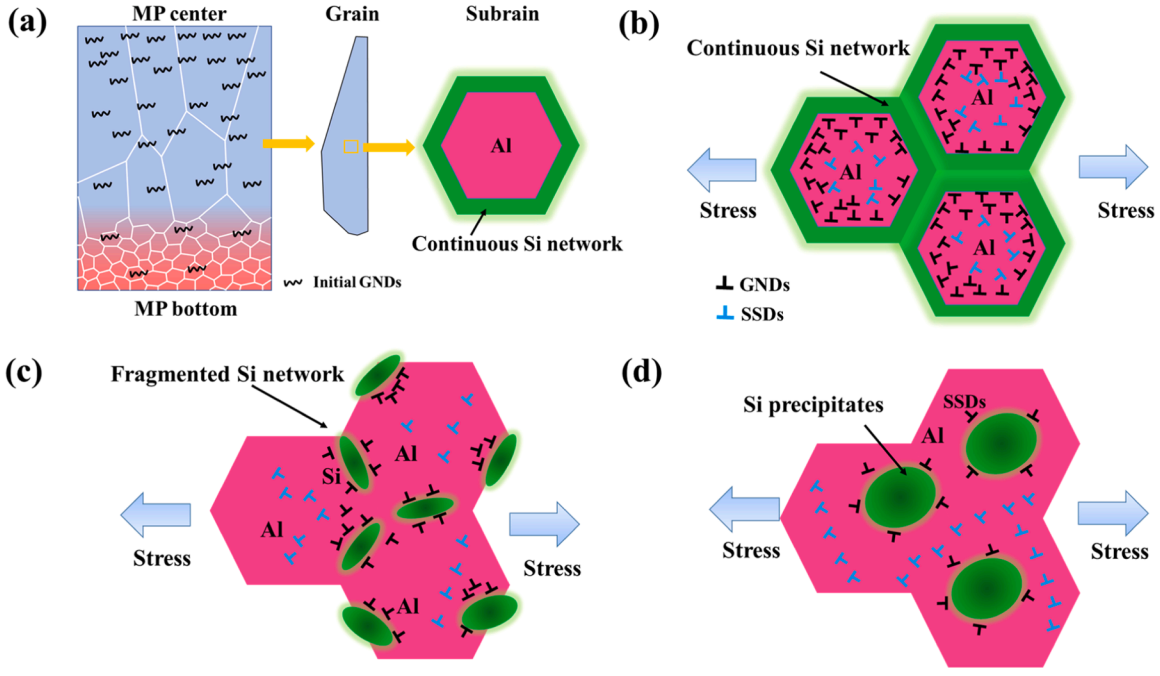

Fig. 11. (a) Schematic illustration of the hierarchically heterogenous structure in the AB sample. (b-d) Subgrain-level illustration of the dislocation distribution upon deformation in the AB (b), SR (c), and ST (d) samples.

microstructure induced the pile-up and accumulation of GNDs at multiple hetero-interfaces, which was a dominant contributor to the excellent strain-hardening ability and thus the high strength of the AB sample. With SR heat treatment, the microstructural heterogeneities were reduced mostly via fragmentation of eutectic phase network due to the consumption of the solute Si in Al cell by coarsening of Si precipitates, leading to less accumulation of GNDs upon deformation. As a result, both GNDs and SSDs contributed to a moderate strain-hardening behavior, leading to the reduction in strength. Further ST heat treatment greatly weakened the heterogeneities at both grain- and subgrain-level, resulting in a low strain-hardening ability mainly caused by the SSDs and thus a significantly reduction in strength. On the other hand, the continuously coarsening of Si precipitates provided less obstacles for dislocation movement, contributing to the increased ductility at a higher temperature. Therefore, this provides the opportunity to tailor the hierarchically heterogeneous microstructure in the AMed AlSi10Mg by carefully tuning the heat treatment procedure, to simultaneously achieve enhanced strain hardening and retain good ductility.

CRediT authorship contribution statement

Jiao Zhang: Software, Resources, Project administration, Methodology, Funding acquisition. **Genqi Tian:** Validation, Resources, Formal analysis, Data curation. **Bo Mao:** Writing – review & editing, Writing – original draft, Funding acquisition, Formal analysis, Data curation, Conceptualization. **Baode Sun:** Supervision, Software, Resources, Project administration, Methodology, Investigation. **Yuqian Wang:** Methodology, Investigation, Formal analysis, Data curation, Conceptualization. **Xing Zhang:** Writing – review & editing, Writing – original draft, Visualization, Project administration, Formal analysis, Data curation. **Sai Chen:** Methodology, Investigation, Formal analysis, Data curation. **Shuangjie Chu:** Methodology, Investigation, Funding acquisition, Formal analysis, Data curation. **Hui Xing:** Supervision, Software, Resources, Formal analysis, Data curation, Conceptualization.

Declaration of Competing Interest

The authors declare that they have no known competing financial interests or personal relationships that could have appeared to influence the work reported in this paper.

Acknowledgement

Bo Mao acknowledgments the funding support from the National Natural Science Foundation of China (Nos. 52101046) and National Key Research and Development Program of China (No. 2022YFB3705602). Jiao Zhang appreciates the funding support from the National Key Research and Development Program of China (No. 2020YFB0311200). Baode Sun thanks the funding support from the National Science Foundation of China (Nos. 51627802 and 51821001).

References

[1] S. Chowdhury, N. Yadaiah, C. Prakash, S. Ramakrishna, S. Dixit, L.R. Gupta, D. Buddhi, Laser powder bed fusion: a state-of-the-art review of the technology, materials, properties & defects, and numerical modelling, J. Mater. Res. Technol. 20 (2022) 2109–2172.
[2] W. Abd-Elaziem, S. Elkatatny, A.-E. Abd-Elaziem, M. Khedr, M.A. Abd El-baky, M. A. Hassan, M. Abu-Okail, M. Mohammed, A. Järvenpää, T. Allam, On the current research progress of metallic materials fabricated by laser powder bed fusion process: a review, J. Mater. Res. Technol. 20 (2022) 681–707.
[3] M. Askari, D.A. Hutchins, P.J. Thomas, L. Astolfi, R.L. Watson, M. Abdi, M. Ricci, S. Laureti, L. Nie, S. Freear, Additive manufacturing of metamaterials: a review, Addit. Manuf. 36 (2020) 101562.
[4] X. Wang, S. Xu, S. Zhou, W. Xu, M. Leary, P. Choong, M. Qian, M. Brandt, Y.M. Xie, Topological design and additive manufacturing of porous metals for bone Scaffolds and orthopaedic implants: a review, Biomaterials 83 (2016) 127–141.
[5] R. Leal, F. Barreiros, L. Alves, F. Romeiro, J. Vasco, M. Santos, C. Marto, Additive manufacturing tooling for the automotive industry, Int. J. Adv. Manuf. Technol. 92 (2017) 1671–1676.
[6] S.A. Tofail, E.P. Koumoulos, A. Bandyopadhyay, S. Bose, L. O'Donoghue, C. Charitidis, Additive manufacturing: scientific and technological challenges, market uptake and opportunities, Mater. Today 21 (2018) 22–37.
[7] A.B. Badiru, V.V. Valencia, D. Liu, Additive Manufacturing Handbook: Product Development for the Defense Industry, CRC Press, 2017.
[8] S.K. Everton, M. Hirsch, P. Stravroulakis, R.K. Leach, A.T. Clare, Review of in-situ process monitoring and in-situ metrology for metal additive manufacturing, Mater. Des. 95 (2016) 431–445.
[9] K. Kempen, L. Thijs, J. Van Humbeeck, J.-P. Kruth, Mechanical properties of AlSi10Mg produced by selective laser melting, Phys. Procedia 39 (2012) 439–446.
[10] A.D. Brandão, J. Gumpinger, M. Gschweitl, C. Seyfert, P. Hofbauer, T. Ghidini, Fatigue properties of additively manufactured AlSi10Mg–surface treatment effect, Proc. Struct. Integr. 7 (2017) 58–66.
[11] M. Tang, P.C. Pistorius, Anisotropic mechanical behavior of AlSi10Mg parts produced by selective laser melting, JOM 69 (2017) 516–522.
[12] T. Rubben, R.I. Revilla, I.De Graeve, Influence of heat treatments on the corrosion mechanism of additive manufactured AlSi10Mg, Corros. Sci. 147 (2019) 406–415.
[13] L. Girelli, M. Tocci, L. Montesano, M. Gelfi, A. Pola, Optimization of heat treatment parameters for additive manufacturing and gravity casting AlSi10Mg alloy. IOP Conference Series, IOP Publishing, 2017.
[14] L. Girelli, M. Tocci, M. Gelfi, A. Pola, Study of heat treatment parameters for additively manufactured AlSi10Mg in comparison with corresponding cast alloy, Mater. Sci. Eng. A 739 (2019) 317–328.
[15] X. Yu, L. Wang, T6 heat-treated AlSi10Mg alloys additive-manufactured by selective laser melting, Proc. Manuf. 15 (2018) 1701–1707.
[16] N.T. Aboulkhair, I. Maskery, C. Tuck, I. Ashcroft, N.M. Everitt, The microstructure and mechanical properties of selectively laser melted AlSi10Mg: the effect of a conventional T6-like heat treatment, Mater. Sci. Eng. A 667 (2016) 139–146.
[17] Z. Li, Z. Li, Z. Tan, D.-B. Xiong, Q. Guo, Stress relaxation and the cellular structure-dependence of plastic deformation in additively manufactured AlSi10Mg alloys, Int. J. Plast. 127 (2020) 102640.
[18] S. Bagherifard, N. Beretta, S. Monti, M. Riccio, M. Bandini, M. Guagliano, On the fatigue strength enhancement of additive manufactured AlSi10Mg parts by mechanical and thermal post-processing, Mater. Des. 145 (2018) 28–41.
[19] Y.M. Wang, T. Voisin, J.T. McKeown, J. Ye, N.P. Calta, Z. Li, Z. Zeng, Y. Zhang, W. Chen, T.T. Roehling, Additively manufactured hierarchical stainless steels with high strength and ductility, Nat. Mater. 17 (2018) 63–71.
[20] Y. Xuan, J. Chang, Y. Ou, R. Yang, Z. Zhang, Heterogeneous structure architected by additive manufacturing: facile route towards strong and ductile steel, Mater. Res. Lett. 12 (2024) 199–207.
[21] P. He, R.F. Webster, V. Yakubov, H. Kong, Q. Yang, S. Huang, M. Ferry, J.J. Kruzic, X. Li, Fatigue and dynamic aging behavior of a high strength Al-5024 alloy fabricated by laser powder bed fusion additive manufacturing, Acta Mater. 220 (2021) 117312.
[22] H.R. Kotadia, G. Gibbons, A. Das, P.D. Howes, A review of laser powder bed fusion additive manufacturing of aluminium alloys: microstructure and properties, Addit. Manuf. 46 (2021) 102155.
[23] Y. Xiao, H. Chen, Z. Bian, T. Sun, H. Ding, Q. Yang, Y. Wu, Q. Lian, Z. Chen, H. Wang, Enhancing strength and ductility of AlSi10Mg fabricated by selective laser melting by TiB2 nanoparticles, J. Mater. Sci. Technol. 109 (2022) 254–266.
[24] N. Limbasiya, A. Jain, H. Soni, V. Wankhede, G. Krolczyk, P. Sahlot, A comprehensive review on the effect of process parameters and post-process treatments on microstructure and mechanical properties of selective laser melting of AlSi10Mg, J. Mater. Res. Technol. (2022).
[25] M.J. Paul, Q. Liu, J.P. Best, X. Li, J.J. Kruzic, U. Ramamurty, B.J.A.M. Gludovatz, Fracture resistance of AlSi10Mg fabricated by laser powder bed fusion, Acta Mater. 211 (2021) 116869.
[26] A. Hadadzadeh, B.S. Amirkhiz, B. Langelier, J. Li, M. Mohammadi, Microstructural consistency in the additive manufactured metallic materials: a study on the laser powder bed fusion of AlSi10Mg, Addit. Manuf. 46 (2021) 102166.
[27] X. Li, X. Wang, M. Saunders, A. Suvorova, L. Zhang, Y. Liu, M. Fang, Z. Huang, T. B. Sercombe, A selective laser melting and solution heat treatment refined Al–12Si alloy with a controllable ultrafine eutectic microstructure and 25% tensile ductility, Acta Mater. 95 (2015) 74–82.
[28] A.I. Mertens, J. Delahaye, J. Lecomte-Beckers, Fusion-based additive manufacturing for processing aluminum alloys: State-of-the-art and challenges, Adv. Eng. Mater. 19 (2017) 1700003.
[29] T. Kimura, T. Nakamoto, Microstructures and mechanical properties of A356 (AlSi7Mg0. 3) aluminum alloy fabricated by selective laser melting, Mater. Des. 89 (2016) 1294–1301.
[30] J. Sun, L. Qiu, F. Wang, Y. Yang, L. Guo, A new modification effect of eutectic si in selective laser melted AlSi10Mg, Mater. Sci. Technol. 35 (2019) 709–715.
[31] H. Xiao, C. Zhang, H. Zhu, Effect of direct aging and annealing on the microstructure and mechanical properties of AlSi10Mg fabricated by selective laser melting, Rapid Prototyp. J. 29 (2023) 118–127.
[32] P. Karimi, E. Sadeghi, J. Ålgårdh, A. Keshavarzkermani, R. Esmaeilizadeh, E. Toyserkani, J. Andersson, Columnar-to-equiaxed grain transition in powder bed fusion via mimicking casting solidification and promoting in situ recrystallization, Addit. Manuf. 46 (2021) 102086.
[33] M.J. Paul, Q. Liu, J.P. Best, X. Li, J.J. Kruzic, U. Ramamurty, B. Gludovatz, Fracture resistance of AlSi10Mg fabricated by laser powder bed fusion, Acta Mater. 211 (2021) 116869.
[34] Y. Zhu, X. Wu, Heterostructured materials, Prog. Mater. Sci. (2022) 101019.
[35] Z. Wang, X. Lin, N. Kang, Y. Hu, J. Chen, W. Huang, Strength-ductility synergy of selective laser melted Al-Mg-Sc-Zr alloy with a heterogeneous grain structure, Addit. Manuf. 34 (2020) 101260.